NOLTA, IEICE

Paper

Excitable multivibrators: Switching dynamics between astable and monostable modes via opto-electronic threshold modulation

Hiroshi Ueno [1], *Hiroshi Kawakami* [2], *and Koichiro Sadakane* [1]

[1] *Faculty of Life and Medical Sciences, Doshisha University*
1-3 Tatara Miyakodani, Kyotanabe, Kyoto 610-0394, Japan

[2] *Self-organization Science Research Center, Doshisha University*
1-3 Tatara Miyakodani, Kyotanabe, Kyoto 610-0394, Japan

Received May 23, 2025; Revised September 1, 2025; Published January 1, 2026

Abstract: Excitation phenomena in nonlinear circuits are realized using light-sensitive multivibrators that alternate between quiescent and oscillatory modes under external illumination. Circuit dynamics are governed by the continuous-time evolution of an analog internal state (capacitor voltage). Simultaneously, the output switches discretely between high and low levels, forming a hybrid system with mixed continuous-discrete behavior. Crucially, the switching threshold is not fixed but modulated by both the output state and the incident light, enabling tunable excitability. A class of such circuits was designed and theoretically analyzed, and their spike-like transient responses were quantitatively verified experimentally. The proposed configuration offers a compact platform for realizing spatially extended excitable media with discrete outputs that continuously evolve.

Key Words: excitable systems, hybrid dynamical systems, relaxation oscillators, nonlinear electronic circuits, multivibrator, opto-electronic feedback

1. Introduction

Many dynamic phenomena observed in nature, biology, and society involve nonlinearities that cannot be captured using linear approximations. In nonlinear science, such phenomena have been understood through the framework of dynamical systems, revealing their universal properties in terms of bifurcations, periodic oscillations, and chaos [1, 2]. In particular, many information processing, regulation, and transmission processes in biological systems are rooted in nonlinear dynamics. Among these, excitability is a hallmark phenomenon characterized by a large transient response elicited by stimuli

DOI: 10.1587/nolta.17.306

exceeding a threshold [3, 4].

To describe such phenomena, the Hodgkin–Huxley model [5] and its reduced form, the FitzHugh-Nagumo (FHN) model [6–8] — also known as the Bonhoeffer–van der Pol (BVP) model — have long been studied as canonical representations of excitable systems. Rooted in the relaxation oscillations of the classical van der Pol oscillator [9, 10], these models embody nonlinearities and time-scale separation (slow–fast dynamics) and admit physical realizations as electronic circuits.

In modern implementations, these excitable dynamics are emulated by circuits combining resonant elements with a nonlinear component — typically a negative differential resistance (e.g., via a negative impedance converter with operational amplifiers). The resulting systems exhibit relaxation oscillations and are naturally framed as hybrid dynamical systems when the fast dynamics are treated as switching between discrete states [11–15].

Physical circuit implementations of excitable systems are attractive for two reasons. First, they enable intuitive, real-time demonstrations of nonlinear dynamics and provide hardware substrates for neuromorphic computing. Second, they scale to real-space networks of locally coupled units with measurable state variables and parameters. Optoelectronic local networks in particular permit explicitly engineered local coupling while maintaining electrical isolation between nodes, avoiding unintended global coupling and enabling intentional wiring of interaction topology. Because each unit is governed by explicit state-space equations (Sec. 2), experimentally observed network motifs can be mapped to operating principles and, in turn, used to guide constructive design. This perspective complements classical mean-field oscillator models such as the Kuramoto framework, which capture collective synchronization under global or all-to-all coupling [16], and photosensitive Belousov-Zhabotinsky (BZ) media, which provide spatially continuous excitable fields for wave propagation and pattern formation [17]. Discrete BZ platforms (droplets/beads) also exist but often face limitations in controllability and reproducibility due to fabrication and delicate setup [18–20]. In contrast, discrete, controllable, and reproducible circuit testbeds based on off-the-shelf components are well-suited for studying locally coupled excitable networks.

We propose and experimentally verify an excitable multivibrator — a simple electronic circuit that switches between oscillatory (astable) and quiescent (monostable) states in response to optical stimulation via a phototransistor-tunable threshold. Unlike prior excitable circuits relying on fixed thresholds or purely electrical control, our design enables real-time light-controlled mode switching with a standard op-amp-based architecture. We position our contribution relative to prior electronic and optoelectronic excitable systems, including FHN-based circuits and photonic/electronic neuron devices [21–27], highlighting that our circuit uses standard components (op-amp, passive elements, phototransistor) and discrete voltage levels — without specialized RTDs or lasers — while uniquely offering optical threshold modulation for immediate mode switching. This minimal, hybrid, slow–fast architecture forms a practical building block for scalable real-space networks of locally coupled excitable units.

2. Theoretical framework

In this section we describe the structure and operating principle of the proposed excitable multivibrator, modeled as a hybrid dynamical system with continuous capacitor voltage and discrete op-amp output states. We then show how optical threshold control yields excitability.

2.1 Basic circuit configuration and operating principle

First, we describe the basic circuit configuration that forms the basis of the present study and explain its operational principles. Figure 1 shows an astable multivibrator implemented with an operational amplifier. In this circuit, capacitor voltage v_C changes depending on whether the output voltage v_o of the op–amp is high or low. The circuit exhibits nonlinear switching behavior, in which the output flips when v_C crosses the reference threshold voltage v_p.

The relevant variables and constants used in this circuit are defined as follows:

- v_o: Output voltage of the op–amp

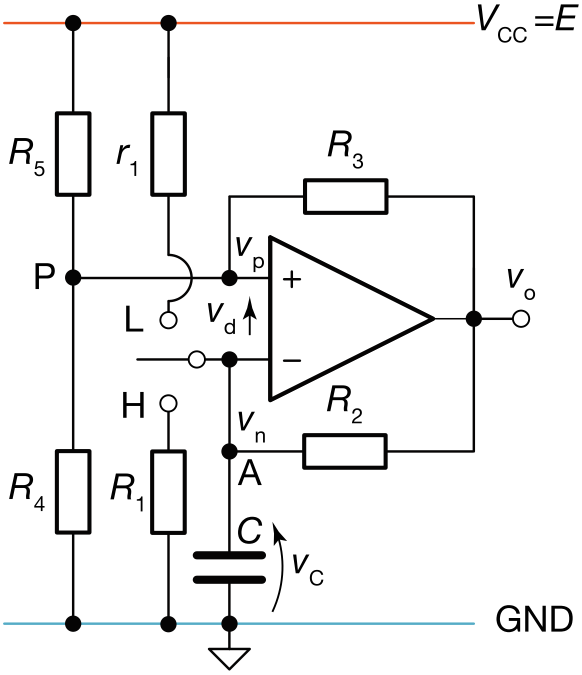

Fig. 1. Electronic circuit diagram of astable and monostable multivibrators using an operational amplifier. R and r denote resistor values, and C denotes the capacitance. The power supply voltage is given by $V_{\mathrm{CC}} = E$. v_{p} and v_{n} represent the voltages at the non-inverting and inverting input terminals of the op–amp, respectively, and v_{o} is the output voltage. The switch connected to the inverting terminal can be either left open or connected to contact L or H.

- v_{C}: Voltage across the capacitor, equivalent to the voltage at the inverting terminal v_{n}
- v_{p}: Voltage at the non-inverting terminal, which serves as a threshold parameter when fixed relative to v_{n}
- R_1-R_5, r_1: Resistors in the circuit
- C: Capacitance of the capacitor

In Fig. 1, the switch connected to the inverting input determines the dynamic regime of the system depending on its position: open, connected to L, or connected to H. These configurations result in distinct dynamical behaviors, as summarized in Table I.

Table I. Switching dynamics of the circuit depending on the position of the switch.

Switch Position	Dynamical Mode	Phase Diagram
Open	Astable	Fig. A-1(b)
Closed on L	Monostable (low)	Fig. A-1(c)
Closed on H	Monostable (high)	Fig. A-1(d)

In the following subsections, we present a theoretical overview of the dynamic behavior associated with each switch configuration. For detailed mathematical derivations, refer to Appendix A.

2.1.1 Switch open: Astable mode

We begin with the case in which the switch is open. Applying Kirchhoff's current law to inverting input terminal A of the op–amp yields the following equation:

$$R_2 C \frac{dv_{\mathrm{C}}}{dt} + v_{\mathrm{C}} = v_{\mathrm{o}}, \tag{1}$$

which governs the slow dynamics of capacitor voltage v_C. The nullcline defined by $dv_\mathrm{C}/dt = 0$ corresponds to $(v_\mathrm{C}, v_\mathrm{o}) = (0, 0)$ or (E, E).

The fast dynamics of output voltage v_o arise from the static and dynamic characteristics of the op–amp. When functioning as a comparator, output v_o can be modeled as an amplification function $a(v_\mathrm{p} - v_\mathrm{C})$ of the differential input $(v_\mathrm{p} - v_\mathrm{C})$. For simplicity, we assume that function behaves as a unit step function:

$$\begin{aligned} v_\mathrm{o} &= a(v_\mathrm{p} - v_\mathrm{C}) \\ &= \mathrm{sign}(v_\mathrm{p} - v_\mathrm{C}), \end{aligned} \tag{2}$$

as shown in Fig. A-1(a) [28]. Because of the parasitic capacitance and phase-compensation elements in the op–amp, the output v_o exhibits non-negligible transient behavior [29]. We adopted a simple model of this dynamic response by introducing a small time constant $\mu \ll 1$, leading to the following first-order differential equation:

$$\mu \frac{dv_\mathrm{o}}{dt} + v_\mathrm{o} = \mathrm{sign}(v_\mathrm{p} - v_\mathrm{C}). \tag{3}$$

Here, μ is a small time constant characterizing the finite response speed of the op–amp output. It originates from the dominant pole formed by the internal compensation capacitor and the effective transconductance, and is further limited by the finite slew rate. Accordingly, the capacitor voltage v_C evolves slowly on the RC time scale $\tau_\mathrm{C} = R_2 C$, whereas the output v_o switches much faster on the scale μ, so that the circuit can be regarded as a typical slow–fast system.

The nullcline, defined by $dv_\mathrm{o}/dt = 0$ corresponds to the static response in Eq. (2). We assume that owing to the fast dynamics, the output transitions instantaneously between $v_\mathrm{o} = 0$ and $v_\mathrm{o} = E$.

The intersection of the two nullclines, located at $v_\mathrm{C} = v_\mathrm{o}$, represents an equilibrium point that is unstable in both directions.

Meanwhile, the voltage v_p at the non-inverting terminal P of the op–amp is given by

$$\begin{aligned} v_\mathrm{p} &= \frac{R_3^{-1} v_\mathrm{o} + R_5^{-1} E}{R_3^{-1} + R_4^{-1} + R_5^{-1}} \\ &\equiv \begin{cases} \alpha E & (\text{if } v_\mathrm{o} = E) \\ \beta E & (\text{if } v_\mathrm{o} = 0) \end{cases} \end{aligned} \tag{4}$$

Combining these dynamics, the system exhibits a four-phase limit cycle involving alternating slow and fast transitions (denoted by "$\rightarrow$" for slow dynamics and "$\twoheadrightarrow$" for fast dynamics):

1. Slow increase in v_C while $v_\mathrm{o} = E$: $v_\mathrm{C} : \beta E \rightarrow \alpha E$
2. Rapid transition in v_o triggered by $v_\mathrm{p} - v_\mathrm{C} = 0$: $v_\mathrm{o} : E \twoheadrightarrow 0$
3. Slow decrease in v_C while $v_\mathrm{o} = 0$: $v_\mathrm{C} : \alpha E \rightarrow \beta E$
4. Rapid transition in v_o again as $v_\mathrm{p} - v_\mathrm{C} = 0$: $v_\mathrm{o} : 0 \twoheadrightarrow E$

Thus, this slow–fast dynamical system [15] is appropriately viewed as a hybrid dynamical system. In other words, it is a mixed-mode system in which the capacitor voltage v_C evolves continuously (analog), whereas the op–amp output v_o switches discretely (digital).

The overall dynamics manifest as a limit cycle illustrated in Fig. A-1(b), consisting of the sequence $\mathrm{a} \rightarrow \mathrm{b} \twoheadrightarrow \mathrm{c} \rightarrow \mathrm{d} \twoheadrightarrow \mathrm{a} \rightarrow \cdots$.

2.1.2 Switch closed on L: Monostable (stable low) mode

When the switch is set to position L, the circuit enters a monostable regime. In this state, the system possesses a single globally stable equilibrium point in the phase space, toward which the system asymptotically converges regardless of the initial conditions.

In this configuration, the capacitor voltage evolves according to the following differential equation:

$$C\frac{dv_{\mathrm{C}}}{dt} + \left(\frac{1}{r_1} + \frac{1}{R_2}\right) v_{\mathrm{C}} = \frac{E}{r_1} + \frac{v_{\mathrm{o}}}{R_2}, \tag{5}$$

Solving for the steady state ($dv_{\mathrm{C}}/dt = 0$), we obtain, for $v_{\mathrm{o}} = 0$,

$$\begin{aligned} {v_{\mathrm{C}}}^* &= \left(\frac{R_2}{r_1 + R_2}\right) E \\ &\equiv \lambda_{\mathrm{L}} E, \end{aligned} \tag{6}$$

which represents a stable fixed point, as illustrated in Fig. A-1(c), provided that the condition $\beta < \lambda_{\mathrm{L}} < \alpha$ holds.

Because of this behavior, we refer to this mode of the monostable multivibrator as the "stable low" mode.

2.1.3 Switch closed on H: Monostable (stable high) mode

Similarly, when the switch is set to position H, the capacitor voltage follows the relation:

$$C\frac{dv_{\mathrm{C}}}{dt} + \left(\frac{1}{R_1} + \frac{1}{R_2}\right) v_{\mathrm{C}} = \frac{v_{\mathrm{o}}}{R_2}, \tag{7}$$

Solving for the steady state ($dv_{\mathrm{C}}/dt = 0$) under $v_{\mathrm{o}} = E$, we get

$$\begin{aligned} {v_{\mathrm{C}}}^* &= \left(\frac{R_1}{R_1 + R_2}\right) E \\ &\equiv \lambda_{\mathrm{H}} E, \end{aligned} \tag{8}$$

which is a stable equilibrium point, as shown in Fig. A-1(d), if $\beta < \lambda_{\mathrm{H}} < \alpha$ is satisfied. This configuration is therefore termed the "stable high" mode.

As shown above, the switching position fundamentally alters the dynamical structure of the circuit, inducing a bifurcation from a limit cycle to relaxation toward a stable equilibrium point. This switch-induced transition is the key mechanism underpinning the design of the excitable multivibrator circuit discussed in the next section.

2.2 Operating principle of the excitable multivibrator

Building on the operational principles described above, we now introduce the essential mechanisms of an *excitable multivibrator*, in which optical stimulation triggers transitions between circuit states. Details on the governing dynamics and required conditions for each configuration are provided in Appendix B.

Excitability refers to a property wherein a system at rest responds to a transient stimulus (such as a brief light pulse) with a large, single spike, and then returns to its resting state.

In the present work, this behavior is realized using an electronic circuit incorporating phototransistors, as exemplified by the LED firefly circuit [28, 30], illustrated in Fig. 2. The excitable circuits designed in this study are classified into four types according to the direction of the threshold modulation (increase or decrease) caused by optical stimulation and the position of the switch (L or H). These types are summarized in Table II. In all cases, the underlying mechanism is the displacement of the fixed point outside the threshold window, thereby inducing a transition from a monostable to an astable regime.

Figure 2(a) shows a configuration in which a phototransistor and resistor r_5 are connected between node P and the supply $V_{\mathrm{CC}} = E$. In Fig. 2(b), a phototransistor and resistor r_4 are connected between node P and ground.

Given these insertion directions, the phototransistor is based solely on the presence or absence of external light, because $V_{\mathrm{CC}} > v_{\mathrm{p}} > 0$ always holds. Thus, we define the conduction state of the phototransistor as a Boolean variable s: $s = 1$ when conducting (illuminated) and $s = 0$ otherwise.

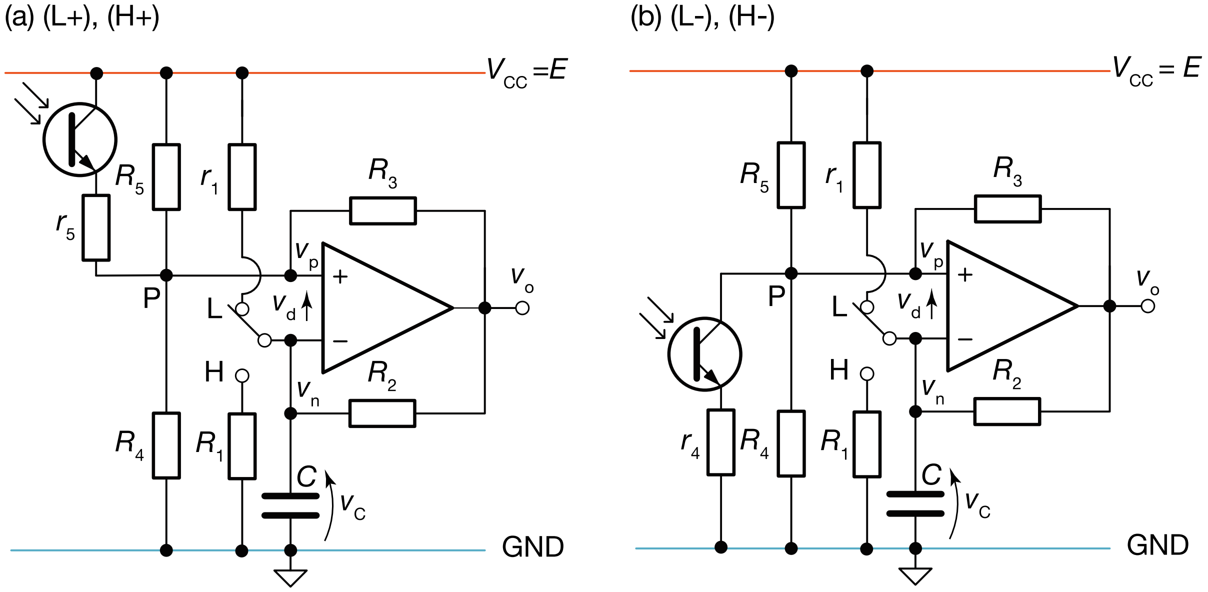

Fig. 2. (a) Circuit of type (+); (b) Circuit of type (−). In (a), a phototransistor and resistor r_5 are connected between node P and the supply voltage $V_{\mathrm{CC}} = E$ in the circuit shown in Fig. 1. In (b), a phototransistor and resistor r_4 are connected between node P and ground, serving as a photosensor for external optical stimulation. When the phototransistor is conducting, R_4 and r_4 form a parallel resistance.

Accordingly, in the conducting state, the circuit in Fig. 2(a) yields a modified threshold parameter via the parallel resistance $R_5 \parallel r_5$, and Fig. 2(b) via $R_4 \parallel r_4$. These threshold parameters are denoted as functions of the conduction state: $\alpha = \alpha(s)$ and $\beta = \beta(s)$. Further details are provided in Appendix B.

The increments in threshold parameters caused by light stimulation are then defined as:

$$\Delta\alpha_{\mathrm{s}} := \alpha(1) - \alpha(0), \quad \Delta\beta_{\mathrm{s}} := \beta(1) - \beta(0).$$

These definitions allow the classification of the circuit types and their behaviors as shown in Table II. L and H denote switch connections to points L and H, respectively.

Table II. Classification of excitable multivibrator circuits. Each circuit exhibits two operational modes — one in darkness, the other under illumination.

Circuit type	In the dark	In the light	$\Delta\alpha_{\mathrm{s}}$	$\Delta\beta_{\mathrm{s}}$
(L+)	Monostable (low)	Astable	+	+
(H+)	Astable	Monostable (high)	+	+
(L−)	Astable	Monostable (low)	−	−
(H−)	Monostable (high)	Astable	−	−

The operating behavior of each circuit type is summarized as follows:

- **(L+)**: Switch connected to L; light increases v_{p} ⇒ spike is induced
- **(H+)**: Switch connected to H; light-off decreases v_{p} ⇒ spike is induced
- **(L−)**: Switch connected to L; light-off increases v_{p} ⇒ spike is induced
- **(H−)**: Switch connected to H; light decreases v_{p} ⇒ spike is induced

In this classification, the (L+) and (H−) types behave as circuits that are quiescent in the dark and oscillatory in response to light-on events. Conversely, the (L−) and (H+) types respond to light-off events, oscillating in darkness and returning to rest under illumination.

Finally, the transition between the modes relies on inequalities that must be satisfied for each circuit to operate as an excitable multivibrator, as listed in Table III.

Table III. Necessary conditions for each circuit type to exhibit excitability.

Circuit type	Prerequisite
(L+)	$\beta(0) < \lambda_{\mathrm{L}} < \beta(1)$
(H+)	$\alpha(0) < \lambda_{\mathrm{H}} < \alpha(1)$
(L−)	$\beta(1) < \lambda_{\mathrm{L}} < \beta(0)$
(H−)	$\alpha(1) < \lambda_{\mathrm{H}} < \alpha(0)$

2.2.1 Comparison of theoretical and classical analyses

For clarity, we note which aspects of the above theoretical analysis are original to this work. The basic multivibrator behavior and slow–fast analysis follow established approaches for relaxation oscillators (e.g., the op amp is modeled as a thresholding comparator as in [28], whereas classical multivibrators were implemented using vacuum tubes [31]). The extension of this analysis to include a light-dependent threshold is also developed in [28, 30]. Relatedly, Amoh *et al.* modeled multivibrators as slow–fast planar systems and experimentally observed canard explosions, clarifying how finite op-amp dynamics govern the continuous onset of relaxation oscillations [15]. However, the excitable switching between modes is performed here for the first time. In particular, the classification of four distinct circuit types with optical switching, as summarized in Table II, goes beyond classical multivibrator theory. This novel theoretical framework highlights how an external photonic stimulus can modulate circuit dynamics, a scenario not addressed in prior studies of multivibrator circuits.

3. Experimental setup

3.1 Circuits

Having established the theoretical design of excitable multivibrator circuits, we now describe the physical components and instrumentation used to construct and experimentally validate these circuits. The resistors used were KOA-brand metal film resistors with a tolerance of ±1%, and the capacitors were ultra-low ESR aluminum electrolytic capacitors from Nippon Chemi–Con, with a tolerance of ±20%. All circuits were assembled on a solderless breadboard for rapid prototyping and testing.

Circuit type (+) was constructed using the following electrical component values:

$$\begin{aligned} R_1 = r_1 &= 150\ \mathrm{k\Omega}, \quad & R_2 &= 100\ \mathrm{k\Omega},\\ R_3 = R_4 &= 330\ \mathrm{k\Omega}, \quad & R_5 &= 1\ \mathrm{M\Omega},\\ r_5 &= 150\ \mathrm{k\Omega}, \quad & C &= 10\ \mu\mathrm{F}. \end{aligned}$$

Circuit type (−) used the same components as circuit (+) except for R_5 and r_4:

$$\begin{aligned} R_1 = r_1 &= 150\ \mathrm{k\Omega}, \quad & R_2 &= 100\ \mathrm{k\Omega},\\ R_3 = R_4 &= 330\ \mathrm{k\Omega}, \quad & R_5 &= 100\ \mathrm{k\Omega},\\ r_4 &= 100\ \mathrm{k\Omega}, \quad & C &= 10\ \mu\mathrm{F}. \end{aligned}$$

All resistor values were selected from the E12 series for ease of procurement, while ensuring that they satisfy the design conditions described later. Capacitance C may be chosen arbitrarily to match the desired measurement time scale. Substituting these component values into Eq. (6) and (8) yield the following equilibrium coefficients:

$$\lambda_{\mathrm{L}} = 0.4, \quad \lambda_{\mathrm{H}} = 0.6.$$

Using Eq. (4) from the theoretical analysis, the corresponding threshold parameters are found to be $\alpha(0) \approx 0.57$, $\alpha(1) \approx 0.78$, $\beta(0) \approx 0.14$ and $\beta(1) \approx 0.56$ for circuit (+), and $\alpha(0) \approx 0.81$, $\alpha(1) = 0.5$, $\beta(0) \approx 0.62$ and $\beta(1) \approx 0.38$ for circuit (−). These values satisfy the necessary conditions listed in Table III for the behavior summarized in Table I.

To satisfy the assumptions in Eq. (2), we employed an NJM2732D operational amplifier (Nisshinbo Micro Devices, formerly JRC), which features rail-to-rail input/output characteristics (also known as full-range or full-swing operation). The optocoupler used to deliver external light stimuli was TLP785 (Toshiba Electronic Devices and Storage Corporation).

3.2 Measurements

The measurements were conducted using two Analog Discovery Studio devices (Digilent), operated in combination. To record three channels of analog voltage signals using the oscilloscope functionality, we employed the dual mode feature of the WaveForms software (Digilent). The oscilloscope probes were connected to capacitor voltage v_C, op–amp output voltage v_o, and threshold voltage v_p, respectively. This setup enabled the observation of the behavior of each circuit from power-up as well as its response to external optical stimulation. All analog waveforms were sampled at 133.203 Hz using the WaveForms oscilloscope setting.

3.3 External optical stimulation

External optical stimulation was delivered via a phototransistor-LED optocoupler. We used Toshiba Electronic Devices & Storage Corporation, TLP785 and followed the specifications in its datasheet [32]. In the time-series experiments, a 5 V drive with a 330 Ω series resistor was applied to the LED to indicate "light-on" intervals, and 15 ms optical pulses were injected at specified timings (Section 4). Detailed absolute irradiance at the phototransistor is fixed by the optocoupler package geometry and was not separately calibrated. See the datasheet for transfer characteristics.

4. Results and discussion

The experimental results obtained for each excitable multivibrator circuits are summarized as follows:

- Circuit (L+): Fig. 3(a),
- Circuit (H+): Fig. 3(b),
- Circuit (L−): Fig. 4(a),
- Circuit (H−): Fig. 4(b).

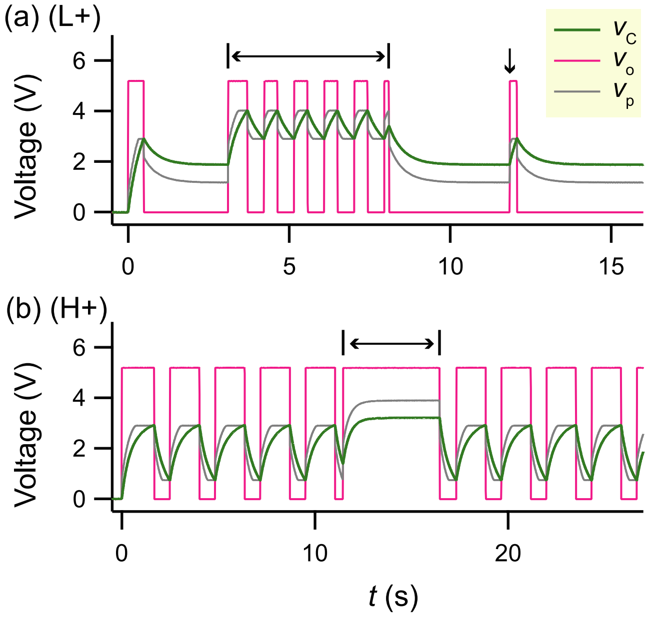

Fig. 3. Time-series waveforms of circuit type (+), as shown in Fig. 1(a). (a) Circuit (L+) corresponding to Fig. B-1, and (b) Circuit (H+) corresponding to Fig. B-2. Each panel displays the capacitor voltage v_C (green), op–amp output voltage v_o (magenta), and threshold voltage v_p (gray). The horizontal double arrow $|\longleftrightarrow|$ bounded by vertical black lines indicates the time window in which a 5 V external optical stimulus is applied (i.e., light-on state). The black downward arrow ↓ denotes the onset of a 15 ms optical pulse.

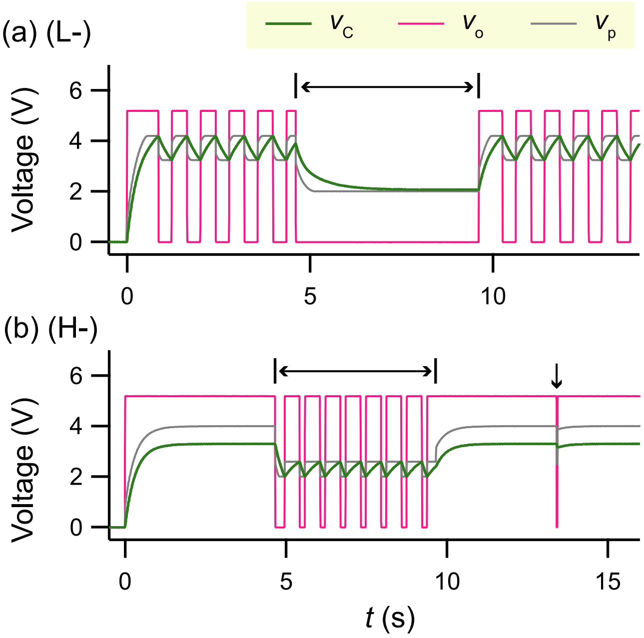

Fig. 4. Time-series waveforms of circuit type (−), as shown in Fig. 1(b). (a) Circuit (L−) corresponding to Fig. B-3, and (b) Circuit (H−) corresponding to Fig. B-4. Each panel displays the capacitor voltage v_{C} (green), op–amp output voltage v_{o} (magenta), and threshold voltage v_{p} (gray). The horizontal double arrow $| \longleftrightarrow |$ bounded by vertical black lines indicates the time window in which a 5 V external optical stimulus is applied (i.e., light-on state). The black downward arrow ↓ denotes the onset of a 15 ms optical pulse.

4.0.1 Common features across all circuits

All four circuit configurations (L+), (H+), (L−), and (H−) share the same excitable mechanism summarized in Table II and analyzed in Sec. 2: a slow–fast hybrid dynamics in which (i) a slow RC charging/discharging process defines the trajectory along a quasi-continuous manifold, while (ii) an op-amp-mediated fast switching event triggers a discrete transition. In all circuits, the output voltage obeys a binary switching law,

$$v_{\mathrm{o}} = \begin{cases} E = 5.0\ \mathrm{V}, & v_{\mathrm{C}} < v_{\mathrm{p}}, \\ 0\ \mathrm{V}, & v_{\mathrm{C}} \geq v_{\mathrm{p}}, \end{cases}$$

and v_{o} undergoes effectively instantaneous transitions whenever the ordering of v_{C} and v_{p} reverses, producing rectangular waveforms (astable operation) or isolated rectangular pulses (monostable operation under brief stimulation). Optical input modulates the effective threshold via the phototransistor — shifting v_{p} with the sign pattern specified in Table II — and thereby controls the onset and cessation of spiking. Consequently, the operating regime differs before and after illumination.

4.0.2 Individual circuit behavior

Consistent with the classification summarized in Table II, the following behaviors were observed for each circuit type.

- **(L+)**: In the dark environment, the capacitor voltage converges to $v_{\mathrm{C}} \simeq \lambda_{\mathrm{L}} E$, indicating a stable low state. Under illumination, the circuit exhibited a limit cycle in which v_{C} transitioned exponentially between the threshold voltages $\beta(1)E$ and $\alpha(1)E$.
- **(H+)**: In the dark, the capacitor voltage exhibits a limit cycle characterized by exponential transitions between $\beta(0)E$ and $\alpha(0)E$. In the bright environment, it asymptotically approached $v_{\mathrm{C}} \simeq \lambda_{\mathrm{H}} E$, corresponding to a stable high state.
- **(L−)**: In the darkness, the circuit exhibits a limit cycle with v_{C} oscillating exponentially between $\beta(0)E$ and $\alpha(0)E$. In the bright environment, the system converged to $v_{\mathrm{C}} \simeq \lambda_{\mathrm{L}} E$, reflecting a

stable low state.

- **(H−)**: In the dark, the circuit approaches $v_{\mathrm{C}} \simeq \lambda_{\mathrm{H}} E$, which is consistent with a stable high state. Under illumination, v_{C} exhibited a limit cycle oscillating between $\beta(1)E$ and $\alpha(1)E$.

These observations confirm that each circuit type behaves as predicted by the theoretical analysis, demonstrating the intended excitable multivibrator functionality. See Appendix Fig. B-1 for (L+), Fig. B-2 for (H+), Fig. B-3 for (L−), and Fig. B-4 for (H−).

4.1 Spiking dynamics

Based on these results, we hypothesize that applying a brief, pulse-like change in ambient illumination induces a spiking oscillation (i.e., an excitable firing event) in the circuits.

This hypothesis was confirmed by the responses of each circuit to a 15 ms optical pulse, as indicated by the black downward arrow (↓) in Figs. 3 and 4. The following theoretical considerations support the above predictions and observations:

1. For the circuit (L+) initially in a dark environment, a brief optical pulse (sub-millisecond to several milliseconds) causes the stable low fixed point to disappear temporarily because of the induced shift into the astable regime. After the stimulus ends and the system returns to the monostable mode, the dynamics converge to a stable equilibrium at $(v_{\mathrm{C}}, v_{\mathrm{o}}) = (\lambda_{\mathrm{L}} E, 0)$.
2. For circuit (H−) in a dark environment, a similar optical pulse temporarily removes the stable high equilibrium and induces a transition to the astable mode. Upon returning to monostability (stable high), the system settles toward the fixed point at $(v_{\mathrm{C}}, v_{\mathrm{o}}) = (\lambda_{\mathrm{H}} E, E)$.

Similarly, when the optical stimulus was briefly turned off for circuits (H+) and (L−) which were initially in a bright environment, the system exhibited an inverted behavior consistent with the above descriptions.

These spiking responses suggest that a desired configuration can be selected depending on the application conditions. Specifically, one may choose between low-side or high-side resting states, and between spiking in response to a transition from dark to light or vice versa.

Thus, the excitable multivibrator has been theoretically designed and experimentally validated.

4.2 Comparison of experimental and theoretical results

4.2.1 Limit cycle behavior in the astable mode

When the switch is connected to the L terminal, the general solution of Eq. (5) is given by

$$\begin{aligned} v_{\mathrm{C}}(t) = {} & \frac{R_2 E + r_1 v_{\mathrm{o}}}{r_1 + R_2} \\ & + \left(v_{\mathrm{C}}(0) - \frac{R_2 E + r_1 v_{\mathrm{o}}}{r_1 + R_2} \right) \exp\left(-\frac{r_1 + R_2}{r_1 R_2 C} t \right) \end{aligned} \tag{9}$$

From this, the period of the limit cycle T is obtained as follows:

For circuit (L+):

$$T = \frac{r_1 R_2 C}{r_1 + R_2} \ln\left[\frac{(\alpha(1) - \lambda_{\mathrm{L}})(\beta(1) - 1)}{(\beta(1) - \lambda_{\mathrm{L}})(\alpha(1) - 1)} \right] \tag{10}$$

For circuit (L−):

$$T = \frac{r_1 R_2 C}{r_1 + R_2} \ln\left[\frac{(\alpha(0) - \lambda_{\mathrm{L}})(\beta(0) - 1)}{(\beta(0) - \lambda_{\mathrm{L}})(\alpha(0) - 1)} \right] \tag{11}$$

Similarly, when the switch is connected to the H terminal, the general solution of Eq. (7) is

$$v_{\mathrm{C}}(t) = \frac{R_1}{R_1 + R_2} v_{\mathrm{o}}$$

$$+\left(v_{\mathrm{C}}(0)-\frac{R_1}{R_1+R_2}v_{\mathrm{o}}\right)\exp\left(-\frac{R_1+R_2}{R_1R_2C}t\right) \tag{12}$$

The corresponding periods are then given as:
For circuit (H+):

$$T=\frac{R_1R_2C}{R_1+R_2}\ln\left[\frac{\alpha(0)(\beta(0)-\lambda_{\mathrm{H}})}{\beta(0)(\alpha(0)-\lambda_{\mathrm{H}})}\right] \tag{13}$$

For circuit (H−):

$$T=\frac{R_1R_2C}{R_1+R_2}\ln\left[\frac{\alpha(1)(\beta(1)-\lambda_{\mathrm{H}})}{\beta(1)(\alpha(1)-\lambda_{\mathrm{H}})}\right] \tag{14}$$

For more details, see Appendix C.

A summary of the theoretical and experimental values of the limit cycle period for each astable circuit is presented in Table IV.

Table IV. Comparison in the astable part of calculated periods T_{calc} with experimental ones T_{exp} for each circuit.

Circuit type	T_{calc} (s)	T_{exp} (s)
(L+)	0.94	0.94(7)
(H+)	2.49	2.31(31)
(L−)	0.78	0.79(7)
(H−)	0.62	0.63(3)

For the experimental period T_{exp}, the frequency f and its uncertainty σ_f were estimated from the peak of the power spectrum obtained via FFT, excluding the first transient cycle and any disturbances owing to optical stimulation. The peak was well-fitted by a Gaussian distribution, and the period was computed as $T_{\mathrm{exp}} = 1/f$ with its uncertainty estimated as $T_{\mathrm{exp}} \cdot \sigma_f/f$. All experimental values agreed with the theoretical predictions within 10% error, and in the cases of circuits (L+), (H+), and (H−), the error was within 1%.

It should also be noted that the fast dynamics of the op–amp output voltage v_{o} were assumed to occur instantaneously, effectively setting their duration to zero in the calculation. The close agreement between the theory and experiment supports the validity of this approximation. Therefore, this slow–fast system can be suitably modeled as a hybrid dynamical system combining analog and digital behaviors, and is potentially useful in applications where symbolic encoding of output states is required.

4.2.2 Relaxation dynamics in the monostable regime

In the monostable parts of Figs. 3 and 4, relaxation toward stable equilibrium points was observed. From these figures, we extracted time windows from 0.43 to 3.10 s in Fig. 3(a), and from 0 to 4.4 s in Fig. 4(b), and compared the theoretical calculations from Eqs. (9), (12) with the fitted values obtained from the experimental results. A comparison is shown in Fig. 5. Table V lists the asymptotic values $v_{\mathrm{C}}(t \to \infty)$ and relaxation times τ obtained from both the theoretical formulas and experimental fitting.

The asymptotic voltage $v_{\mathrm{C}}(t \to \infty)$ exhibits an error of approximately 10%, whereas the relaxation time τ exhibits a deviation of approximately 30–50%. Nevertheless, as shown in Fig. 5, the relaxation curves from the experimental data were well-fitted by theoretical models. These discrepancies were within reasonable bounds, considering the tolerance levels of the resistors and capacitors used.

Therefore, the theoretical circuit models presented above are experimentally validated.

4.3 Results synthesis and implications

Across all four configurations, optical threshold modulation deterministically toggled the operating mode between monostable rest and astable oscillation, and brief illumination elicited single spike-like

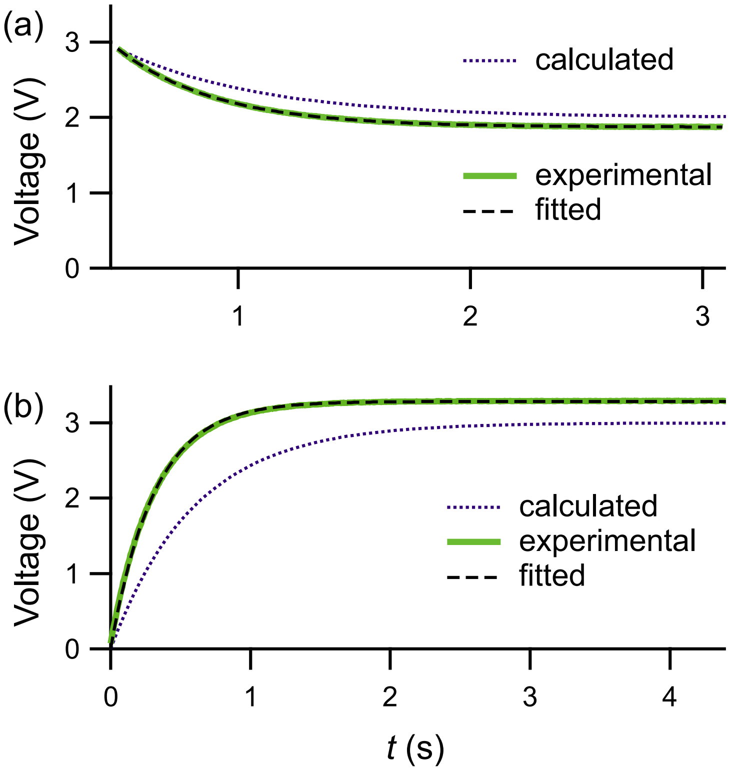

Fig. 5. Comparison of the calculations with the experimental results in relaxations to the equilibrium points e and f. (a) The green line is the experimental result excerpted from Fig. 3(a) between $t \approx 0.2$ and 3.1 seconds. The dotted curve shows the calculated waveform using Eq. (9) with nominal component values, while the dashed black curve is the best fit using the same equation. (b) The green line is the experimental result excerpted from Fig. 4(b) between $t = 0$ and approximately 4 seconds. The dotted curve shows the theoretical calculation using Eq. (12), and the dashed black curve represents the best fit to the experimental data.

Table V. Comparison in the monostable part for circuits (L+) and (H−) of the calculated capacitor voltage at infinity $v_{\mathrm{C}}(\infty)$ and its relaxation time τ with fitted values.

Circuit type	$v_{\mathrm{C}}(\infty)$ (V)		τ (s)	
	Calculation	Fitted	Calculation	Fitted
(L+)	2.00	1.87(1)	0.60	0.43(1)
(H−)	3.00	3.28(1)	0.60	0.31(1)

transients from rest (Secs. 4.0.1, 4.1). Quantitatively, astable periods and monostable relaxations matched analytical predictions within expected tolerance bands (period errors within $\sim 10\%$, three types within $\sim 1\%$; relaxation time deviations ~ 30–50% attributable to component tolerances and parasitics), validating the slow–fast hybrid description and the assumption of effectively instantaneous switching (Sec. 4.2; see also Fig. 5).

These results fulfill the design objective stated in the Introduction — real-time light-controlled switching between quiescent and oscillatory states in a simple slow–fast multivibrator built from standard components —and motivate applications such as light-gated event detectors, optical-to-spike encoders, and locally coupled excitable arrays. We elaborate on these directions in Sec. 4.4 and consolidate our conclusions in Sec. 5.

4.4 Perspectives

The spike-generation capabilities of the proposed circuits suggest several potential applications in neuromorphic electronics and optical sensing. For instance, an excitable multivibrator unit could be used as a light-gated event detector, emitting a spike output only when a sufficient illumination is received (and remaining quiescent otherwise). It could also function as an analog optical-to-spike encoder, converting continuous input light signals into discrete spiking patterns. Furthermore, by optoelectronically coupling many such excitable units, one could construct a distributed excitable medium or neural network analog, in which spike pulses propagate through an array of light-connected nodes. Such a system would serve as a hardware platform for studying excitable wave propagation or for implementing neuromorphic computations. These future avenues highlight the broader impact of achieving excitability with optical control, opening possibilities for novel light-responsive, essentially clock-free computing and sensing systems.

Because the proposed excitable unit operates in continuous time and emits spikes only upon threshold-crossing events, it naturally supports clock-free, event-driven computation. This operating mode is aligned with neuromorphic principles that emphasize asynchronous, sparse, and low-latency encoding [33]. Recent demonstrations further indicate that networks of physical spiking elements can realize real-time computation without a global clock: photonic spiking neurons exhibit bio-realistic excitability and collective, computation-relevant synchronization dynamics [34]; event-driven optoelectronic neurons achieve femtojoule-level spiking and integrate sensing with spike generation [35]; and an asynchronous sensing–computing neuromorphic SoC performs real-time processing with sub-milliwatt power by activating only on input events [36]. Taken together, these results support our claim that arrays of the present optically gated excitable multivibrators can provide a physically grounded substrate for clockless, real-time information processing at the edge.

5. Conclusions

We have demonstrated a simple, optically controlled excitable multivibrator that switches in real time between monostable and astable modes, with quantitative agreement supporting a slow–fast hybrid description.

The nonlinear dynamics of astable and monostable operational amplifier multivibrator circuits were investigated both theoretically and experimentally. These circuits, serving as representative implementations of rectangular-wave oscillators using operational amplifiers, were described as hybrid dynamical systems incorporating both hysteresis comparators and RC circuits, characteristic of relaxation oscillators. Whether the circuit exhibits astable or monostable behavior (stable low/high) is determined solely by the relationship between the bifurcation points defined by the threshold parameters and nullcline of the capacitor.

In this study, such control was realized by introducing synthetic resistances modulated by the presence or absence of external light stimuli incident on the phototransistor. Moreover, it was theoretically demonstrated, along with practical circuit implementations, that this mechanism allows the construction of four types of excitable multivibrators by switching between astable and monostable regimes. Oscilloscope-based experimental measurements substantiated these theoretical predictions. In summary, the goal of achieving a light-controllable excitable multivibrator has been fulfilled by the presented design, as evidenced by its successful switching between modes under optical input.

Although the static characteristic of the operational amplifier was approximated using a unit step function in this study, it can alternatively be described by a differentiable function such as tanh [15]. Such a model would enable numerical simulation of the circuit dynamics.

Furthermore, the framework presented in this study can be extended to construct bistable multivibrators. In the circuits shown in Fig. 1, connecting the negative terminal of the op–amp to both the L and H terminals and tuning parameters such as R_1, r_1, R_3, R_4, R_5, r_4, and r_5 would allow such bistable operation. Applying a suitable triggering stimulus could yield flip-flop-like behavior.

The proposed circuit is expected to serve as a building block for the excitable units in future applications. By optoelectronically coupling multiple excitable units, a discretized excitable medium can be realized. This serves as an analog model for neural dynamics and cardiac tissues. Compared with classical excitable media such as the photosensitive Belousov-Zhabotinsky reaction [17], the present system provides highly reproducible experiments with controllable parameters.

Looking forward, the excitable multivibrator concept could be implemented in integrated photonic or semiconductor platforms to achieve faster and more compact neuromorphic hardware. For example, on-chip light sources and detectors could replicate the phototransistor behavior, enabling ultrafast (nanosecond-scale) optical triggering and potential integration into large-scale excitable arrays. Additionally, the simple architecture also lends itself to VLSI integration for creating large-scale excitable networks. Furthermore, the circuit's optical responsiveness without clock suggests applications in real-time sensing, where the circuit could serve as a front-end element that converts incident light stimuli directly into electrical spike signals for subsequent processing.

Acknowledgments

The authors thank Professor Yoshikawa at Doshisha University for valuable discussions. HU wishes to acknowledge the warm support of the Yoshida Scholarship Foundation for the "Doctor 21" program.

Author declarations

Conflict of Interest

The authors have no conflicts to disclose.

Data Availability Statement

Data supporting the findings of this study, including circuit measurements and theoretical calculations, are available from the corresponding author upon reasonable request.

Author Contributions

H. Ueno and H. Kawakami contributed to the conceptualization and theoretical analysis. H. Ueno and H. Kawakami designed and constructed the circuits. H. Ueno and K. Sadakane conducted data acquisition and analysis. H. Ueno and K. Sadakane wrote the original draft of the manuscript. K. Sadakane revised the manuscript and provided supervision throughout the project. All authors reviewed and approved the final version of the manuscript.

Appendix

A. Basic dynamics of the multivibrator circuit

This appendix provides a theoretical description of the dynamic characteristics exhibited by the circuit depending on the switch configuration.

A.0.1 Case with the switch open: Astable mode

First, when the switch is open, applying Kirchhoff's current law at the inverting input terminal A of the operational amplifier yields

$$R_2 C \frac{dv_\mathrm{C}}{dt} + v_\mathrm{C} = v_\mathrm{o} \tag{A-1}$$

In addition, for voltage v_p at the non-inverting input terminal P of the operational amplifier,

$$\frac{v_\mathrm{o} - v_\mathrm{p}}{R_3} + \frac{-v_\mathrm{p}}{R_4} + \frac{E - v_\mathrm{p}}{R_5} = 0 \tag{A-2}$$

Solving this equation for v_p gives

$$\begin{aligned} v_\mathrm{p} &= \frac{R_3^{-1} v_\mathrm{o} + R_5^{-1} E}{R_3^{-1} + R_4^{-1} + R_5^{-1}} \\ &\equiv \begin{cases} \alpha E & (\text{if } v_\mathrm{o} = E) \\ \beta E & (\text{if } v_\mathrm{o} = 0) \end{cases} \end{aligned} \tag{A-3}$$

Here,

$$\alpha = \frac{R_3^{-1} + R_5^{-1}}{R_3^{-1} + R_4^{-1} + R_5^{-1}} \tag{A-4}$$

(a) (v_p, v_C)-v_o (b) v_C-v_o : astable

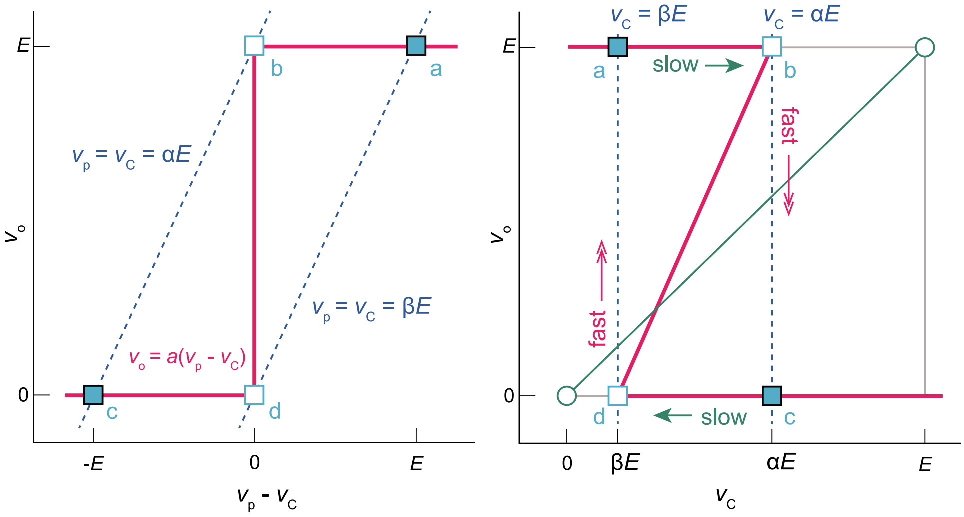

(c) v_C-v_o : monostable (stable low) (d) v_C-v_o : monostable (stable high)

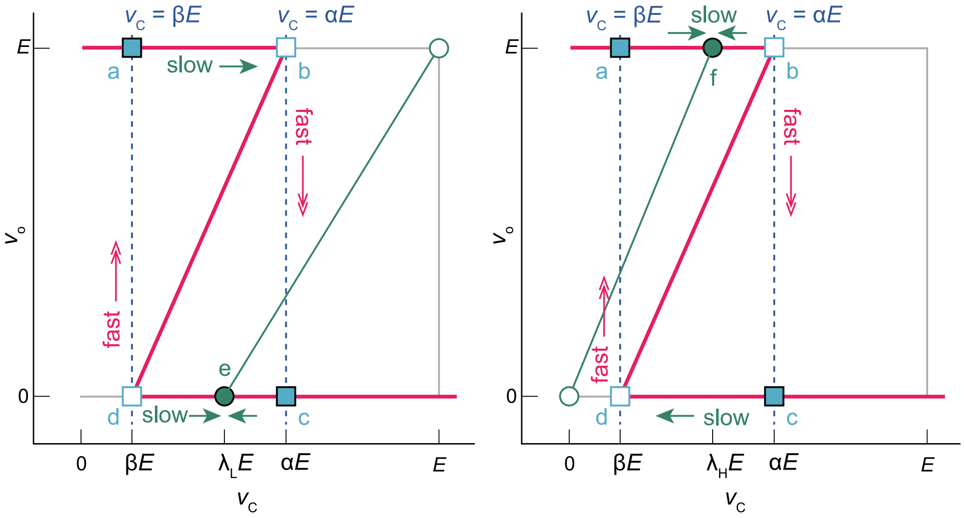

Fig. A-1. Schematic relationship between v_C and v_o in (a) v_d-v_o plane and represented in (b)-(d) $v_C - v_o$ plane for (b) astable multivibrator, (c) monostable multivibrator (stable low), (d) monostable multivibrator (stable high). The thick red lines represent the nullclines for the output voltage of the operational amplifier. The solid green curve corresponds to the capacitor voltage v_C nullcline with the switch open, and the dotted green line corresponds to that when the switch is closed on the L side. Points b and d (white-outlined blue squares) mark the starting points of rapid transitions in v_o due to tangent bifurcations; a and c (solid blue squares) are their corresponding arrival points. Points e and f (green-filled circles) indicate stable equilibrium points.

$$\beta = \frac{R_5^{-1}}{R_3^{-1} + R_4^{-1} + R_5^{-1}} \tag{A-5}$$

are defined as above.

Next, we consider the static characteristics of the operational amplifier. Using the approach proposed by Kosaka et al. [28], the output voltage v_o of the operational amplifier is modeled as a unit step function of the differential input voltage $v_p - v_C$ as follows:

$$\begin{aligned} v_o &= a(v_p - v_C) \\ &= \operatorname{sign}(v_p - v_C) \end{aligned} \tag{A-6}$$

This results in a set of operating points for the operational amplifier, as shown in Fig. A-1(a). The relationship between v_C and v_o is shown in Fig. A-1(b).

Next, we consider the dynamic characteristics of the operational amplifier. The output voltage v_{o} varies with time owing to the parasitic and phase-compensation capacitors [29]. Here, we adopt a minimal model of this behavior using a first-order differential equation with a small parameter $\mu \ll 1$:

$$\mu \frac{dv_{\mathrm{o}}}{dt} + v_{\mathrm{o}} = \mathrm{sign}(v_{\mathrm{p}} - v_{\mathrm{C}}) \tag{A-7}$$

The equilibrium set of this equation for the fast dynamics of v_{o} relative to v_{C} corresponds to the operating points of the operational amplifier, as shown in Fig. A-1(b). This system exhibits hysteresis, with points b and d corresponding to tangential bifurcation points. Since no stable fixed point exists in Fig. A-1(b), the state of the system evolves periodically.

A.0.2 Case with the switch closed on the L side: Monostable (stable low) mode

Consider the circuit in Fig. 1 with the switch thrown to the contact point L, such that resistor r_1 connects the power supply V_{CC} to the inverting input terminal of the operational amplifier.

With respect to the voltage $v_n = v_{\mathrm{C}}$ at the inverting input terminal, the following differential equation is obtained from the relationship between the currents through resistors r_1 and R_2 and their voltage drops, the capacitor charge-voltage relation, and Kirchhoff's current law at the inverting terminal:

$$C\frac{dv_{\mathrm{C}}}{dt} = \frac{E - v_{\mathrm{C}}}{r_1} + \frac{v_{\mathrm{o}} - v_{\mathrm{C}}}{R_2} \tag{A-8}$$

Therefore, the ordinary differential equation governing the slow variable v_{C} is given by:

$$C\frac{dv_{\mathrm{C}}}{dt} + \left(\frac{1}{r_1} + \frac{1}{R_2}\right) v_{\mathrm{C}} = \frac{E}{r_1} + \frac{v_{\mathrm{o}}}{R_2} \tag{A-9}$$

From Eq. (A-9), setting $dv_{\mathrm{C}}/dt = 0$ yields the steady-state value $v_{\mathrm{C}} = v_{\mathrm{C}}^* = \lambda_{\mathrm{L}} E$.
Here,

$$\lambda_{\mathrm{L}} = \frac{R_2}{r_1 + R_2} \tag{A-10}$$

is defined as shown.

The behavior of the non-inverting terminal voltage v_{p}, as well as the static and dynamic characteristics of the operational amplifier, are the same as in the case where the switch is open. In Fig. A-1(c), the nullcline for the fast dynamics of the operational amplifier (red line) and that for the slow capacitor dynamics (green dotted line) intersect only at point e $(v_{\mathrm{C}}, v_{\mathrm{o}}) = (\lambda_{\mathrm{L}} E, 0)$, provided that $\beta < \lambda_{\mathrm{L}} < \alpha$ holds. This point is the globally unique stable equilibrium of the system.

A.0.3 Case with the switch closed on the H side: Monostable (stable high) mode

Consider the circuit in Fig. 1 with the switch thrown to contact point H, such that resistor R_1 connects the inverting input terminal of the operational amplifier to the ground.

$$C\frac{dv_{\mathrm{C}}}{dt} + \frac{v_{\mathrm{C}}}{R_1} = \frac{v_{\mathrm{o}} - v_{\mathrm{C}}}{R_2} \tag{A-11}$$

Therefore, the ordinary differential equation governing the slow variable v_{C} is given by:

$$C\frac{dv_{\mathrm{C}}}{dt} + \left(\frac{1}{R_1} + \frac{1}{R_2}\right) v_{\mathrm{C}} = \frac{v_{\mathrm{o}}}{R_2} \tag{A-12}$$

From Eq. (A-12), setting $dv_{\mathrm{C}}/dt = 0$ yields the steady-state value $v_{\mathrm{C}} = v_{\mathrm{C}}^* = \lambda_{\mathrm{H}} E$.
Here,

$$\lambda_{\mathrm{H}} = \frac{R_1}{R_1 + R_2} \tag{A-13}$$

is defined as shown.

The behavior of the non-inverting terminal voltage v_{p}, as well as the static and dynamic characteristics of the operational amplifier, are the same as in the case where the switch is open.

In Fig. A-1(d), the nullcline for the fast dynamics of the operational amplifier (red line) and the nullcline for the slow capacitor dynamics (green dotted line) intersect only at point f $(v_{\mathrm{C}}, v_{\mathrm{o}}) = (\lambda_{\mathrm{H}}E, E)$, provided that $\beta < \lambda_{\mathrm{H}} < \alpha$ holds.

This point is the globally unique stable equilibrium of the system.

B. Dynamics of the excitable multivibrator

B.1 Increasing threshold parameter: the circuit as "(+)"

Figure 2 (a) shows a circuit in which a phototransistor and resistor r_5 are connected between node P and power supply $V_{\mathrm{CC}} = E$ in Fig. 1. When the collector side of the phototransistor is connected to the power supply, $V_{\mathrm{CC}} > v_{\mathrm{p}}$ always holds; therefore, conduction depends solely on the presence or absence of external light. Therefore, we define the conduction state s of the phototransistor as a Boolean variable. In other words, the conducting state induced by external light stimulation is defined as $s = 1$, and the non-conducting state is defined as $s = 0$. According to Kirchhoff's current law at node P, following the same logic as that in Eqs. (A-2) and (A-3), we obtain.

$$v_{\mathrm{p}} = \begin{cases} \alpha(s)E & (\text{if } v_{\mathrm{o}} = E) \\ \beta(s)E & (\text{if } v_{\mathrm{o}} = 0) \end{cases} \tag{B-1}$$

$$\alpha(s)E = \frac{R_3^{-1} + R_5^{-1} + sr_5^{-1}}{R_3^{-1} + R_4^{-1} + R_5^{-1} + sr_5^{-1}} \tag{B-2}$$

$$\beta(s)E = \frac{R_5^{-1} + sr_5^{-1}}{R_3^{-1} + R_4^{-1} + R_5^{-1} + sr_5^{-1}} \tag{B-3}$$

These expressions describe the dependence of v_{p} on the conduction state s. From these expressions, the threshold parameters of circuit (+) are calculated as follows: $\beta(0) \sim 0.14$, $\beta(1) \sim 0.56$, $\alpha(0) \sim 0.57$, $\alpha(1) \sim 0.78$. The values are obtained for each state.

That is, because $\beta(0) < \beta(1)$ and $\alpha(0) < \alpha(1)$, the threshold parameters increase in response to external light stimulation.

B.1.1 When the switch is closed to the L side: (L+)

The parameters $\lambda_{\mathrm{L}} = 0.4$, $\beta(0) \sim 0.14$, and $\beta(1) \sim 0.56$ satisfy the condition $\beta(0) < \lambda_{\mathrm{L}} < \beta(1)$, meaning that the equilibrium point is located between the threshold values.

The dynamics of this (L+) circuit are as shown in Fig. B-1.

In a bright environment, when $v_{\mathrm{o}} = 0$, the threshold voltage increases from $v_{\mathrm{p}} = \beta(0)E$ to $v_{\mathrm{p}} = \beta(1)E$, causing the unique stable equilibrium point $\mathrm{e}(v_{\mathrm{C}}, v_{\mathrm{o}}) = (\lambda_{\mathrm{L}}E, 0)$ to disappear.

Therefore, as shown in Table II, the circuit behaves as a monostable (stable low) circuit in the dark and is astable in the light.

B.1.2 When the switch is closed to the H side: (H+)

We consider the circuit in which the switch in Fig. 2(a) is flipped to the H contact, thereby connecting the inverting terminal of the op–amp to the ground through resistor R_1.

The given parameters $\lambda_{\mathrm{H}} = 0.6$, $\alpha(0) \sim 0.57$, and $\alpha(1) \sim 0.78$ satisfy the inequality $\alpha(0) < \lambda_{\mathrm{H}} < \alpha(1)$, indicating that the equilibrium point lies between the two threshold values. The dynamics of the (H+) circuit are shown in Fig. B-2. When $v_{\mathrm{o}} = E$, as the threshold voltage decreases from $v_{\mathrm{p}} = \alpha(1)E$ in the bright environment to $v_{\mathrm{p}} = \alpha(0)E$ in the dark, the unique stable equilibrium point $\mathrm{f}(v_{\mathrm{C}}, v_{\mathrm{o}}) = (\lambda_{\mathrm{H}}E, E)$ vanishes. Thus, this circuit behaves as astable in the dark and monostable (stable high) in the bright (see Table II).

B.2 Decreasing threshold parameter: the circuit as "(−)"

As shown in Fig. 2(b), the phototransistor becomes conductive under external light stimulation, forming a combined resistance of $R_4 \parallel r_4$.

Then, similar to Eq. (A-2) and (A-3), Kirchhoff's current law applied to node P yields.

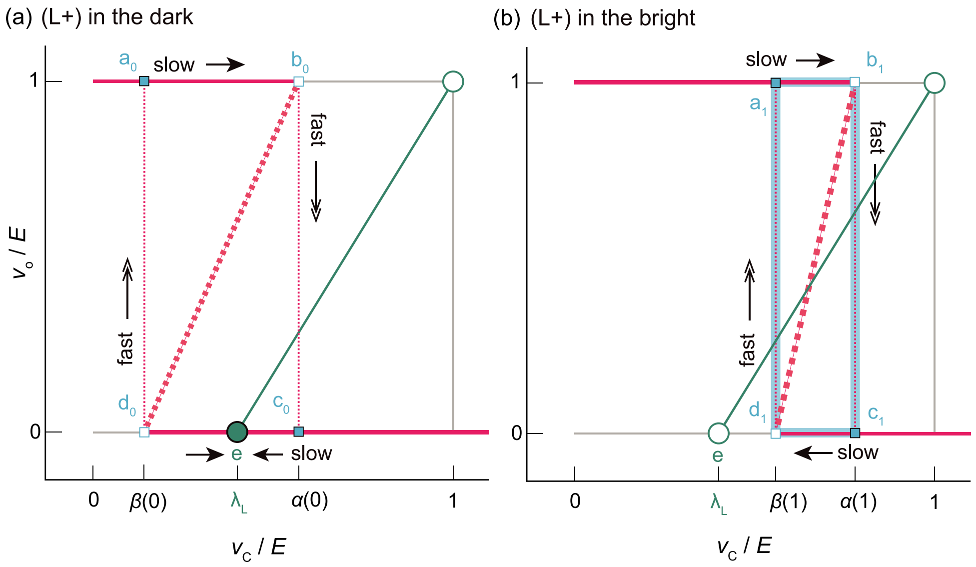

Fig. B-1. Dynamics of the (L+) circuit. (a) Dark environment without external light stimulus; (b) Bright environment with external light stimulus. The horizontal axis represents the capacitor voltage v_{C}, and the vertical axis the output voltage v_{o}. All voltages are normalized by the supply voltage E. The nullcline of the fast dynamics of the op–amp output v_{o} is shown with red solid and dashed lines, forming a Z-shaped nullcline. The vertical red dotted lines indicate the threshold parameters (tangential bifurcation points) where mode transitions occur. In the dark, $v_{\mathrm{C}}/E = \alpha(0)$ and $v_{\mathrm{C}}/E = \beta(0)$; in the light, $v_{\mathrm{C}}/E = \alpha(0)$ and $v_{\mathrm{C}}/E = \beta(1)$. The green solid line represents the nullcline for the slow dynamics of the capacitor voltage v_{C}. In (a), the green-filled circle at point $\mathrm{e}(\lambda_{\mathrm{L}}, 0)$ represents the intersection of the nullclines of the op–amp and the capacitor (a stable fixed point). In (b), the thick light-blue rectangle indicates the limit cycle followed by $(v_{\mathrm{C}}, v_{\mathrm{o}})$, tracing the trajectory $\mathrm{a}_1 \to \mathrm{b}_1 \to \mathrm{c}_1 \to \mathrm{d}_1 \to \mathrm{a}_1 \to \cdots$.

$$\begin{cases} v_{\mathrm{p}} = \alpha(s)E & (\text{if } v_{\mathrm{o}} = E) \\ v_{\mathrm{p}} = \beta(s)E & (\text{if } v_{\mathrm{o}} = 0) \end{cases} \tag{B-4}$$

Where

$$\alpha(s) = \frac{R_3^{-1} + R_5^{-1}}{R_3^{-1} + R_4^{-1} + R_5^{-1} + sr_4^{-1}} \tag{B-5}$$

$$\beta(s) = \frac{R_5^{-1}}{R_3^{-1} + R_4^{-1} + R_5^{-1} + sr_4^{-1}} \tag{B-6}$$

By substituting the values of the resistors, the threshold parameters for the (−) circuit are obtained as: $\beta(0) \simeq 0.6226$, $\beta(1) \simeq 0.3837$, $\alpha(0) \simeq 0.811$, $\alpha(1) = 0.5$ Therefore, since $\beta(0) > \beta(1)$ and $\alpha(0) > \alpha(1)$, the threshold parameters decrease under external light stimulation.

B.2.1 When the switch is closed to the L side: (L-)

We consider the case where the switch in Fig. 2 (b) is turned to the L contact, connecting resistor r_1 between the power supply V_{CC} and the inverting input of the operational amplifier. The slow state v_{C} related to the capacitor follows the same dynamics as the circuit (L+) (see §. B.1.1), and is governed by Eq. (A-9), thus yielding $v_C^* = \lambda_{\mathrm{L}}E$.

The given parameters $\lambda_{\mathrm{L}} = 0.4$, $\beta(0) \simeq 0.6226$, and $\beta(1) \simeq 0.3837$ satisfy the inequality $\beta(1) < \lambda_{\mathrm{L}} < \beta(0)$. When $v_{\mathrm{o}} = 0$, the threshold voltage increases from $v_{\mathrm{p}} = \beta(1)E$ in the bright environment to $v_{\mathrm{p}} = \beta(0)E$ in the dark, causing the unique stable equilibrium point $\mathrm{f}(v_{\mathrm{C}}, v_{\mathrm{o}}) = (\lambda_{\mathrm{L}}E, 0)$ to vanish. The behavior of this circuit (L-) is illustrated in Fig. B-3. As shown in Table II, the circuit is astable in the dark environment, and monostable (stable low) in a bright environment.

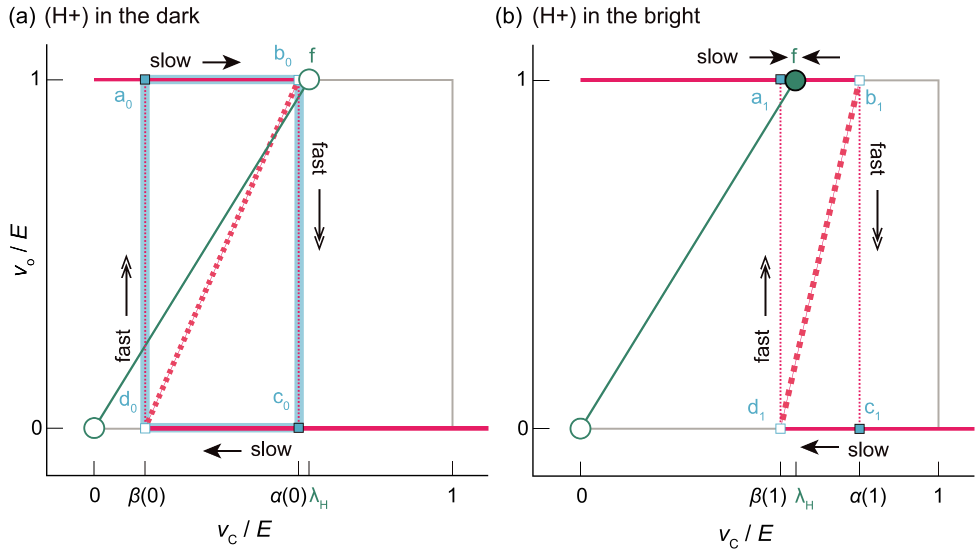

Fig. B-2. Dynamics of the (H+) circuit: (a) dark environment without external light stimulus, and (b) bright environment under external light stimulus. The horizontal axis is the capacitor voltage v_C, and the vertical axis represents the output voltage v_o, both normalized by the supply voltage E. The fast dynamics nullcline of the op–amp output voltage v_o is represented by red solid and dashed lines, forming a Z-shaped nullcline. The vertical red dotted lines indicate the threshold parameters corresponding to mode transitions (tangent bifurcation points). In (a) for the dark environment, $v_\mathrm{C}/E = \alpha(0)$ and $v_\mathrm{C}/E = \beta(0)$; in (b) for the bright environment, $v_\mathrm{C}/E = \alpha(1)$ and $v_\mathrm{C}/E = \beta(1)$. The green solid line represents the nullcline of the slow dynamics of the capacitor voltage v_C. In (a), the light-blue bold rectangle indicates the limit cycle of $(v_\mathrm{C}, v_\mathrm{o})$, tracing the orbit $\mathrm{a}_0 \to \mathrm{b}_0 \to \mathrm{c}_0 \to \mathrm{d}_0 \to \mathrm{a}_0 \to \cdots$. In (b), the green-filled circle at point $\mathrm{f}(\lambda_\mathrm{H}, 1)$ marks the intersection of the nullclines of the op–amp and capacitor, representing a stable equilibrium point.

B.2.2 When the switch is closed to the H side: (H-)

We consider the case where the switch in Fig. 2 (b) is turned to the H contact, connecting resistor R_1 between the inverting input of the operational amplifier and the GND. The slow variable v_C for the capacitor follows the same dynamics as in circuit (H+) (B.1.2), and is given by Eq. (A-12), thus yielding $v_C^* = \lambda_\mathrm{H} E$.

With $\lambda_\mathrm{H} = 0.6$, $\alpha(0) \simeq 0.811$, and $\alpha(1) = 0.5$, the inequality $\alpha(1) < \lambda_\mathrm{H} < \alpha(0)$ is actually satisfied. Therefore, when $v_\mathrm{o} = E$, the threshold voltage decreases from $v_\mathrm{p} = \alpha(0)E$ in the dark to $v_\mathrm{p} = \alpha(1)E$, causing the unique stable fixed point $\mathrm{f}(v_\mathrm{C}, v_\mathrm{o}) = (\lambda_\mathrm{H} E, E)$ to disappear. The dynamics of this circuit (H-) are shown in Fig. B-4. Thus, the circuit is monostable (stable high) in the dark and astable in the bright environment.

Table II summarizes the behaviors of all four circuits discussed so far.

C. Theoretical limit cycle periods

We theoretically derive the period T of the limit cycle and compare it with the experimental results.

First, we assume that the fast dynamics of the operational amplifier output voltage v_o occur instantaneously and that the elapsed time can be approximated as zero.

C.1 Switch open: Astable

First, we consider the simplest circuit case, in which the switch is open as shown in Fig. 1. The slow dynamics of the capacitor voltage v_C follow Eq. (A-1).

The motion along segment ab in Fig. A-1(b), where $v_\mathrm{o} = E$, is determined by the solution of the equation

$$R_2 C \frac{dv_\mathrm{C}}{dt} + v_\mathrm{C} = E \tag{C-1}$$

Thus, we calculate the time T_1 required for the system to evolve from point a ($v_\mathrm{C} = \beta E$) to point

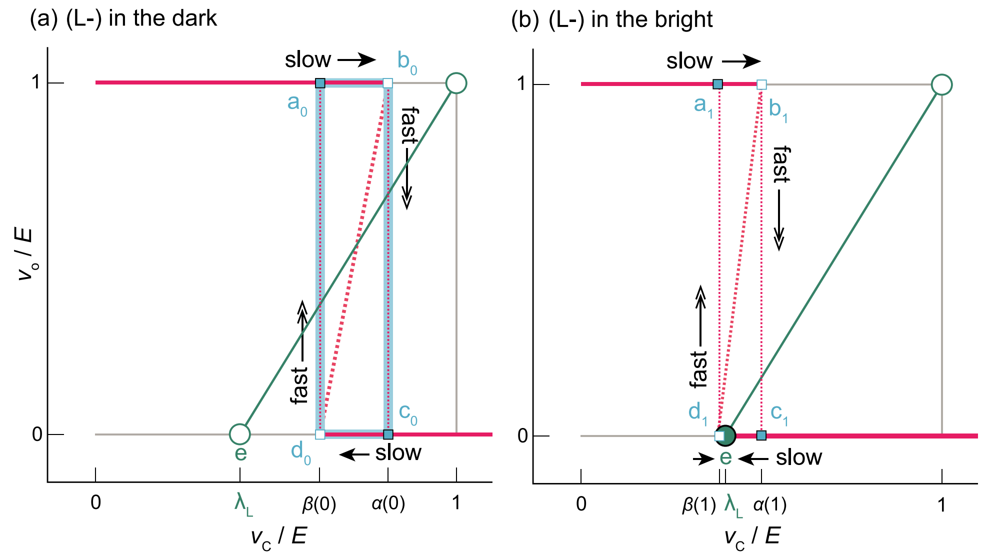

(a) (L-) in the dark

(b) (L-) in the bright

Fig. B-3. The dynamics of circuit (L-) are (a) a dark environment without external light stimulation and (b) a bright environment under illumination. The horizontal axis represents capacitor voltage v_{C}, and the vertical axis represents output voltage v_{o}, normalized by supply voltage E. nullclines for the fast dynamics of v_{o} are shown as red solid and dashed lines. These form a Z-shaped nullcline structure. Vertical red dotted lines indicate bifurcation thresholds for mode transitions (tangent bifurcation points). (a) In the dark environment, $v_{\mathrm{C}}/E = \alpha(0)$ and $v_{\mathrm{C}}/E = \beta(0)$, (b) In the bright environment, $v_{\mathrm{C}}/E = \alpha(0)$ and $v_{\mathrm{C}}/E = \beta(0)$. The green solid line is the nullcline of the slow capacitor dynamics. In (a), the cyan rectangle represents the limit cycle traced by $(v_{\mathrm{C}}, v_{\mathrm{o}})$, which follows the trajectory $\mathrm{a}_0 \to \mathrm{b}_0 \to \mathrm{c}_0 \to \mathrm{d}_0 \to \mathrm{a}_0 \to \cdots$. In (b), the green filled circle at point $\mathrm{e}(\lambda_{\mathrm{L}}, 0)$ is the unique intersection of the operational amplifier and capacitor nullclines, representing a stable equilibrium point.

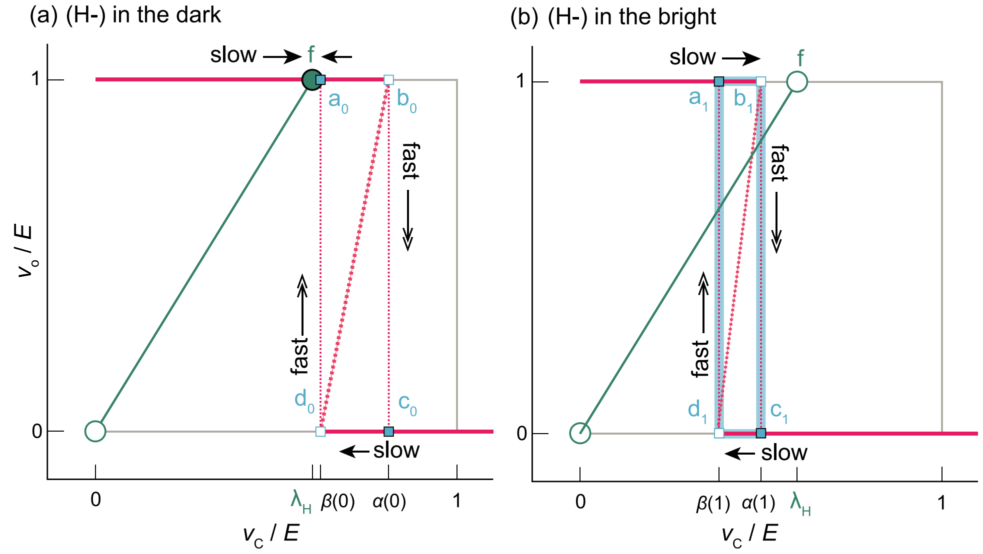

(a) (H-) in the dark

(b) (H-) in the bright

Fig. B-4. Dynamics of circuit (H-): (a) dark environment without external light stimulation and (b) bright environment under illumination. The horizontal axis represents the capacitor voltage v_{C}, and the vertical axis represents the output voltage v_{o}, both normalized by the supply voltage E. Nullclines for the fast dynamics of v_{o} are shown in red solid and dashed lines, respectively. This forms a Z-shaped nullcline. The vertical red dotted line indicates the threshold parameter for mode transition (tangent bifurcation point). (a) In a dark environment, $v_{\mathrm{C}}/E = \alpha(0)$ and $v_{\mathrm{C}}/E = \beta(0)$, (b) In a bright environment, $v_{\mathrm{C}}/E = \alpha(0)$ and $v_{\mathrm{C}}/E = \beta(0)$. The green solid line represents the nullcline for the slow dynamics of v_{C}. In (a), the green-filled circle at point $\mathrm{f}(\lambda_{\mathrm{H}}, 1)$ represents the intersection of the amplifier and capacitor nullclines (stable equilibrium point). In (b), the thick cyan rectangle indicates the limit cycle of $(v_{\mathrm{C}}, v_{\mathrm{o}})$ tracing the trajectory $\mathrm{a}_1 \to \mathrm{b}_1 \to \mathrm{c}_1 \to \mathrm{d}_1 \to \mathrm{a}_1 \to \cdots$.

b ($v_C = \alpha E$).

The solution $v_C(t)$ with the initial condition $v_C(0) = \beta E$ is

$$v_C(t) = E + (\beta - 1)E \exp\left(-\frac{t}{R_2 C}\right) \tag{C-2}$$

Hence, we determine T_1 by imposing the condition $v_C(T_1) = \alpha E$.

$$T_1 = R_2 C \ln \frac{\beta - 1}{\alpha - 1} \tag{C-3}$$

Similarly, the time T_2 required for motion along segment cd is given by:

$$T_2 = R_2 C \ln \frac{\alpha}{\beta} \tag{C-4}$$

Therefore, the period $T = T_1 + T_2$ of the limit cycle shown in Fig. A-1(b) is given by:

$$T = R_2 C \ln \frac{\alpha(\beta - 1)}{\beta(\alpha - 1)} \tag{C-5}$$

C.2 Switch L closed: Monostable (stable low)

Similarly, when switch L is closed, the time evolution of capacitor voltage $v_C(t)$ starting from $v_C(0)$ at time $t = 0$ is given by Eq. (A-9):

$$\begin{aligned} v_C(t) = &\frac{R_2 E + r_1 v_o}{r_1 + R_2} \\ &+ \left(v_C(0) - \frac{R_2 E + r_1 v_o}{r_1 + R_2}\right) \exp\left(-\frac{r_1 + R_2}{r_1 R_2 C} t\right) \end{aligned} \tag{C-6}$$

Therefore, the time t at which $v(t) = v_p$ can be obtained analytically.

When $v_o = E$

$$t = \frac{r_1 R_2 C}{r_1 + R_2} \ln \frac{v_C(0) - E}{v_p - E} \tag{C-7}$$

When $v_o = 0$

$$t = \frac{r_1 R_2 C}{r_1 + R_2} \ln \frac{v_C(0) - \lambda_L E}{v_p - \lambda_L E} \tag{C-8}$$

By substituting the state of v_o, threshold parameter v_p, and the initial value $v_C(0)$ into these two equations, the limit cycles of circuits (L+) and (L-) can be determined.

C.2.1 Limit cycle of circuit (L+)

In the case of circuit (L+), as shown in Fig. B-1, panel (b), time T_1 for the transition from point a$_1$ ($v_C = \beta(1)E$) to point b$_1$ ($v_C = \alpha(1)E$), and time T_2 for the transition from point c$_1$ ($v_C = \alpha(1)E$) to point d$_1$ ($v_C = \beta(1)E$) are given by the following equations:

$$T_1 = \frac{r_1 R_2 C}{r_1 + R_2} \ln \left(\frac{\beta(1) - 1}{\alpha(1) - 1}\right) \tag{C-9}$$

$$T_2 = \frac{r_1 R_2 C}{r_1 + R_2} \ln \left(\frac{\alpha(1) - \lambda_L}{\beta(1) - \lambda_L}\right) \tag{C-10}$$

$$\begin{aligned} T &= T_1 + T_2 \\ &= \frac{r_1 R_2 C}{r_1 + R_2} \ln \left[\frac{(\alpha(1) - \lambda_L)(\beta(1) - 1)}{(\beta(1) - \lambda_L)(\alpha(1) - 1)}\right] \end{aligned} \tag{C-11}$$

By substituting $r_1 = 150\ \mathrm{k\Omega}$, $R_2 = 100\ \mathrm{k\Omega}$, $\lambda_L = 0.4$, $\beta(1) \approx 0.5585$, $\alpha(1) \approx 0.7793$, and $C = 10\,\mu\mathrm{F}$ into the above, we obtain $T \approx 0.94$.

C.2.2 Limit cycle of circuit (L-)

Similarly, in the case of circuit (L-), as shown in Fig. B-3, panel (a), time T_1 for the transition from point a_0 ($v_\mathrm{C} = \beta(0)E$) to point b_0 ($v_\mathrm{C} = \alpha(0)E$), and time T_2 for the transition from point c_0 ($v_\mathrm{C} = \alpha(0)E$) to point d_0 ($v_\mathrm{C} = \beta(0)E$) are given by the following equations:

$$T_1 = \frac{r_1 R_2 C}{r_1 + R_2} \ln \left(\frac{\beta(0) - 1}{\alpha(0) - 1} \right) \tag{C-12}$$

$$T_2 = \frac{r_1 R_2 C}{r_1 + R_2} \ln \left(\frac{\alpha(0) - \lambda_\mathrm{L}}{\beta(0) - \lambda_\mathrm{L}} \right) \tag{C-13}$$

$$\begin{aligned} T &= T_1 + T_2 \\ &= \frac{r_1 R_2 C}{r_1 + R_2} \ln \left[\frac{(\alpha(0) - \lambda_\mathrm{L})(\beta(0) - 1)}{(\beta(0) - \lambda_\mathrm{L})(\alpha(0) - 1)} \right] \end{aligned} \tag{C-14}$$

By substituting $r_1 = 150\ \mathrm{k\Omega}$, $R_2 = 100\ \mathrm{k\Omega}$, $\lambda_\mathrm{L} = 0.4$, $\beta(0) \approx 0.6226$, $\alpha(0) \approx 0.811$, and $C = 10\,\mu\mathrm{F}$, we obtain $T \approx 0.78$.

C.3 Switch H closed: Monostable (stable high)

Similarly, $v_\mathrm{C}(t)$ is given by Eq. (A-12):

$$\begin{aligned} v_\mathrm{C}(t) = &\frac{R_1}{R_1 + R_2} v_\mathrm{o} \\ &+ \left(v_\mathrm{C}(0) - \frac{R_1}{R_1 + R_2} v_\mathrm{o} \right) \exp \left(-\frac{R_1 + R_2}{R_1 R_2 C} t \right) \end{aligned} \tag{C-15}$$

When $v_\mathrm{o} = E$:

$$t = \frac{R_1 R_2 C}{R_1 + R_2} \ln \frac{v_\mathrm{C}(0) - \lambda_\mathrm{H} E}{v_\mathrm{p} - \lambda_\mathrm{H} E} \tag{C-16}$$

When $v_\mathrm{o} = 0$:

$$t = \frac{R_1 R_2 C}{R_1 + R_2} \ln \frac{v_\mathrm{C}(0)}{v_\mathrm{p}} \tag{C-17}$$

By substituting the state of v_o, threshold parameter v_p, and initial value $v_\mathrm{C}(0)$ into these two equations, the limit cycles of circuits (H+) and (H-) can be determined.

C.3.1 Limit cycle of circuit (H+)

In the case of circuit (H+), from Fig. B-2(a), the time T_1 taken for the trajectory from point a_0 ($v_\mathrm{C} = \beta(0)E$) to point b_0 ($v_\mathrm{C} = \alpha(0)E$), and the time T_2 from point c_0 ($v_\mathrm{C} = \alpha(0)E$) to point d_0 ($v_\mathrm{C} = \beta(0)E$), are given as follows:

$$T_1 = \frac{R_1 R_2 C}{R_1 + R_2} \ln \left(\frac{\beta(0) - \lambda_\mathrm{H}}{\alpha(0) - \lambda_\mathrm{H}} \right) \tag{C-18}$$

$$T_2 = \frac{R_1 R_2 C}{R_1 + R_2} \ln \left(\frac{\alpha(0)}{\beta(0)} \right) \tag{C-19}$$

$$\begin{aligned} T &= T_1 + T_2 \\ &= \frac{R_1 R_2 C}{R_1 + R_2} \ln \left[\frac{\alpha(0)(\beta(0) - \lambda_\mathrm{H})}{\beta(0)(\alpha(0) - \lambda_\mathrm{H})} \right] \end{aligned} \tag{C-20}$$

By substituting $R_1 = 150\ \mathrm{k\Omega}$, $R_2 = 100\ \mathrm{k\Omega}$, $\lambda_\mathrm{H} = 0.6$, $\beta(0) \sim 0.1416$, $\alpha(0) \sim 0.5708$, and $C = 10\ \mu\mathrm{F}$ into the equation, the result is $T \simeq 2.49$.

C.3.2 Limit cycle of circuit (H-)

In the case of circuit (H-), as shown in Fig. B-4, the time T_1 taken for the trajectory from point a_1 ($v_\mathrm{C} = \beta(1)E$) to point b_1 ($v_\mathrm{C} = \alpha(1)E$), and the time T_2 from point c_1 ($v_\mathrm{C} = \alpha(1)E$) to point d_1 ($v_\mathrm{C} = \beta(1)E$) are given as follows:

$$T_1 = \frac{R_1 R_2 C}{R_1 + R_2} \ln\left(\frac{\beta(1) - \lambda_\mathrm{H}}{\alpha(1) - \lambda_\mathrm{H}}\right) \tag{C-21}$$

$$T_2 = \frac{R_1 R_2 C}{R_1 + R_2} \ln\left(\frac{\alpha(1)}{\beta(1)}\right) \tag{C-22}$$

$$\begin{aligned} T &= T_1 + T_2 \\ &= \frac{R_1 R_2 C}{R_1 + R_2} \ln\left[\frac{\alpha(1)(\beta(1) - \lambda_\mathrm{H})}{\beta(1)(\alpha(1) - \lambda_\mathrm{H})}\right] \end{aligned} \tag{C-23}$$

By substituting $R_1 = 150$ kΩ, $R_2 = 100$ kΩ, $\lambda_\mathrm{H} = 0.6$, $\beta(1) \simeq 0.3837$, $\alpha(1) = 0.5$, and $C = 10$ μF into the equation, we obtain $T \simeq 0.62$.

References

[1] S. Strogatz, *Nonlinear Dynamics and Chaos: With Applications to Physics, Biology, Chemistry, and Engineering*, A Chapmann & Hall Book, Boca Raton: CRC Press, Taylor & Francis Group, third edition ed., 2024.

[2] S. Strogatz, *SYNC: How Order Emerges from Chaos in the Universe, Nature, and Daily Life*, New York, NY: Hyperion, 1. paperback ed ed., 2003.

[3] E.M. Izhikevich, "Neural Excitability, Spiking and Bursting," *International Journal of Bifurcation and Chaos*, vol. 10, pp. 1171–1266, June 2000.

[4] E.M. Izhikevich, *Dynamical Systems in Neuroscience*, MIT Press, 2007.

[5] A.L. Hodgkin and A.F. Huxley, "A quantitative description of membrane current and its application to conduction and excitation in nerve," *The Journal of Physiology*, vol. 117, pp. 500–544, August 1952.

[6] R. FitzHugh, "Mathematical models of threshold phenomena in the nerve membrane," *The Bulletin of Mathematical Biophysics*, vol. 17, pp. 257–278, December 1955.

[7] R. Fitzhugh, "Impulses and Physiological States in Theoretical Models of Nerve Membrane," *Biophysical Journal*, vol. 1, pp. 445–466, July 1961.

[8] J.-I. Nagumo, S. Arimoto, and S. Yoshizawa, "An Active Pulse Transmission Line Simulating Nerve Axon," *Proc. IRE*, vol. 50, pp. 2061–2070, October 1962.

[9] B. van der Pol, "LXXXVIII. On "relaxation-oscillations"," *The London, Edinburgh, and Dublin Philosophical Magazine and Journal of Science*, vol. 2, pp. 978–992, November 1926.

[10] B. van der Pol and J. van der Mark, "Frequency Demultiplication," *Nature*, vol. 120, pp. 363–364, September 1927.

[11] Y. Ma, S. Mizuochi, and T. Kousaka, "A method of systematic analysis of hybrid dynamical systems, and its application in power electronics," *2006 IEEE International Conference on Industrial Technology*, pp. 1966–1971, December 2006.

[12] Y. Ma, H. Kawakami, C.K. Tse, and T. Kousaka, "General consideration for modeling and bifurcation analysis of switched dynamical systems," *International Journal of Bifurcation and Chaos*, vol. 16, pp. 693–700, March 2006.

[13] D. Ito, T. Ueta, T. Kousaka, J. Imura, and K. Aihara, "Controlling Chaos of Hybrid Systems by Variable Threshold Values," *International Journal of Bifurcation and Chaos*, vol. 24, p. 1450125, October 2014.

[14] Y. Miino, T. Ueta, and H. Kawakami, "Nonlinear resonance and devil's staircase in a forced planer system containing a piecewise linear hysteresis," *Chaos, Solitons & Fractals*, vol. 111, pp. 75–85, June 2018.

[15] S. Amoh, T. Ueta, and H. Kawakami, “Transient Responses to Relaxation Oscillations in Multivibrators,” *IEEE Access*, vol. 12, pp. 471–482, 2024.

[16] Y. Kuramoto, “Self-entrainment of a population of coupled non-linear oscillators,” *International Symposium on Mathematical Problems in Theoretical Physics* (H. Araki, ed.), (Berlin, Heidelberg), pp. 420–422, Springer Berlin Heidelberg, 1975.

[17] L. Kuhnert, K.I. Agladze, and V.I. Krinsky, “Image processing using light-sensitive chemical waves,” *Nature*, vol. 337, pp. 244–247, January 1989.

[18] K. Gizynski and J. Gorecki, “Chemical memory with states coded in light controlled oscillations of interacting Belousov–Zhabotinsky droplets,” *Physical Chemistry Chemical Physics*, vol. 19, no. 9, pp. 6519–6531, 2017.

[19] M. Kuze, Y. Hiranishi, Y. Okamoto, A. Shioi, and S. Nakata, “Coupling of Two Microbeads Exhibiting Different Features of Oscillations in the Belousov-Zhabotinsky Reaction,” *Chemistry Letters*, vol. 48, pp. 847–850, June 2019.

[20] I.L. Mallphanov and V.K. Vanag, “Fabrication of New Belousov–Zhabotinsky Micro-Oscillators on the Basis of Silica Gel Beads,” *The Journal of Physical Chemistry A*, vol. 124, pp. 272–282, January 2020.

[21] S. Binczak, S. Jacquir, J.-M. Bilbault, V.B. Kazantsev, and V.I. Nekorkin, “Experimental study of electrical FitzHugh–Nagumo neurons with modified excitability,” *Neural Networks*, vol. 19, pp. 684–693, June 2006.

[22] Z.T. Njitacke, J. Ramadoss, C.N. Takembo, K. Rajagopal, and J. Awrejcewicz, “An enhanced FitzHugh–Nagumo neuron circuit, microcontroller-based hardware implementation: Light illumination and magnetic field effects on information patterns,” *Chaos, Solitons & Fractals*, vol. 167, p. 113014, February 2023.

[23] R. Ahsan, Z. Wu, S.A.A. Jalal, and R. Kapadia, “Ultralow Power Electronic Analog of a Biological Fitzhugh–Nagumo Neuron,” *ACS Omega*, vol. 9, pp. 18062–18071, April 2024.

[24] W. Zhang, M. Hejda, Q.R.A. Al-Taai, D. Owen-Newns, B. Romeira, J.M.L. Figueiredo, J. Robertson, E. Wasige, and A. Hurtado, “Photonic-electronic spiking neuron with multi-modal and multi-wavelength excitatory and inhibitory operation for high-speed neuromorphic sensing and computing,” *Neuromorphic Computing and Engineering*, vol. 4, p. 044006, November 2024.

[25] M. Hejda, E. Malysheva, Q.R.A. Al-Taai, E. Wasige, V. Dolores-Calzadilla, J. Figueiredo, B. Romeira, and A. Hurtado, “Artificial optoelectronic spiking neurons with laser-coupled resonant tunnelling diode systems,” *2022 IEEE Photonics Conference (IPC)*, pp. 1–2, 13-17 November 2022.

[26] I. Ortega, O. Piro, J. Figueiredo, B. Romeira, and J. Javaloyes, “Spike propagation in a nanolaser-based optoelectronic neuron,” *2021 Conference on Lasers and Electro-Optics Europe & European Quantum Electronics Conference (CLEO/Europe-EQEC)*, p. 1, June 2021.

[27] J.M. Martins, S.V. Gurevich, and J. Javaloyes, “Excitability and memory in a time-delayed optoelectronic neuron,” *Physical Review Applied*, vol. 22, p. 024050, August 2024.

[28] T. Kousaka, H. Kawakami, and T. Ueta, “Synchronization of Electric Fireflies by Using Square Wave Generators,” *IEICE Trans. Fundamentals of Electronics, Communications and Computer Sciences*, vol. 81, pp. 656–663, April 1998.

[29] J. Karki, “Effect of Parasitic Capacitance in Op Amp Circuits,” *Technical Report SLOA013A*, Dallas, TX, 2000.

[30] M. Sekikawa, A. Tsuji, K. Kimoto, I. Aihara, D. Ito, T. Ueta, K. Aihara, and H. Kawakami, “Optically coupled oscillators (OCOs) – LED fireflies,” *Proc. 20th ACM International Conference on Multimedia - MM ’12*, (Nara, Japan), p. 1485, ACM Press, 2012.

[31] A.A. Andronov, A.A. Vitt, and S.E. Khaikin, *Theory of Oscillators*, Adiwes International Series in Physics, Pergamon, January 1966.

[32] Toshiba Electronic Devices & Storage Corporation, “Photocoupler TLP785 datasheet,” 2019.

[33] G. Indiveri and T.K. Horiuchi, “Frontiers in Neuromorphic Engineering,” *Frontiers in Neuroscience*, vol. 5 – 2011, 2011.

[34] T. Inagaki, K. Inaba, T. Leleu, T. Honjo, T. Ikuta, K. Enbutsu, T. Umeki, R. Kasahara, K.

Aihara, and H. Takesue, “Collective and synchronous dynamics of photonic spiking neurons,” *Nature Communications*, vol. 12, p. 2325, April 2021.

[35] Y.-J. Lee, M.B. On, X. Xiao, R. Proietti, and S.J.B. Yoo, “Photonic spiking neural networks with event-driven femtojoule optoelectronic neurons based on Izhikevich-inspired model,” *Optics Express*, vol. 30, pp. 19360–19389, May 2022.

[36] M. Yao, O. Richter, G. Zhao, N. Qiao, Y. Xing, D. Wang, T. Hu, W. Fang, T. Demirci, M. De Marchi, L. Deng, T. Yan, C. Nielsen, S. Sheik, C. Wu, Y. Tian, B. Xu, and G. Li, “Spike-based dynamic computing with asynchronous sensing-computing neuromorphic chip,” *Nature Communications*, vol. 15, p. 4464, May 2024.